Environmental Science & Technology

pubs.acs.org/est

Article

Elevated Mercury Deposition, Accumulation, and Migration in a Karst Forest

Hu Du, Xun Wang,* Wei Yuan, Fei Wu, Longyu Jia, Nantao Liu, Che-Jen Lin, Jiang Gan, Fuping Zeng, Kelin Wang, and Xinbin Feng

Cite This: *Environ. Sci. Technol.* 2023, 57, 17490−17500

Read Online

ACCESS | Metrics & More | Article Recommendations | Supporting Information

ABSTRACT: The karst forest is one of the extremely sensitive and fragile ecosystems in southwest China, where the biogeochemical cycling of mercury (Hg) is largely unknown. In this study, we investigated the litterfall deposition, accumulation, and soil migration of Hg in an evergreen-deciduous broadleaf karst forest using high-resolution sampling and stable isotope techniques. Results show that elevated litterfall Hg concentrations and fluxes in spring are due to the longer lifespan of evergreen tree foliage exposed to atmospheric Hg^0. The hillslope has 1−2 times higher litterfall Hg concentration compared to the low-lying land due to the elevated atmospheric Hg levels induced by topographical and physiological factors. The Hg isotopic model suggests that litterfall Hg depositions account for ∼80% of the Hg source contribution in surface soil. The spatial trend of litterfall Hg deposition cannot solely explain the trend of Hg accumulation in the surface soil. Indeed, soil erosion enhances Hg accumulation in soil of low-lying land, with soil Hg concentration up to 5-times greater than the concentration on the hillslope. The high level of soil Hg migration in the karst forest poses significant ecological risks to groundwater and downstream aquatic ecosystems.

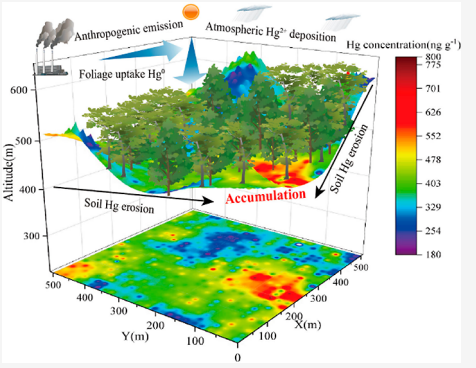

KEYWORDS: *mercury deposition, mercury accumulation, mercury migration, karst forest, soil*

Downloaded via CHENGDU DOCUM AND INFO CTR on March 29, 2024 at 08:03:39 (UTC).
See https://pubs.acs.org/sharingguidelines for options on how to legitimately share published articles.

1. INTRODUCTION

Mercury (Hg) and its compounds are neurotoxic and cause significant health impacts on the global ecosystems and humans.[1] More than 95% of Hg in the atmosphere exists as elemental Hg vapor (Hg^0) with a residence time of 0.3−1.5 years.[2−5] Atmospheric Hg^0 deposition is the most dominant Hg source in terrestrial ecosystems.[5−10] Forest has been regarded as the largest atmospheric elemental Hg^0 sink globally with an annual deposition of 1000−2400 Mg.[3,9,11] Thus, understanding atmospheric Hg sequestration and migration in forests is the foundation for assessing Hg accumulation and induced ecological risks.

The karst region of southwest China is one of the three primary karst areas in the world.[12] The relatively shallow and discontinuous soil layers, extensive rock exposure, and water leakage of karst ecosystems lead to extremely sensitive and fragile ecology.[12−14] Therefore, karst forests may exhibit a unique Hg biogeochemical cycling in contrast to other forest ecosystems.[15−20] This hypothesis is based upon the heterogeneity of the rocky landscape, discontinuous vegetation covers, and soil layers[12−14] that alter the soil chemistry and atmospheric deposition spatially. In addition, the highly fragmented carbonate rock landscape is prone to erosion[13,21] and therefore accelerates soil Hg migration with runoff and leaching.[22]

The complexity of the karst landscape and hydrological processes[12−14] present challenges in tracing the sources, accumulation, and migration of Hg. To adequately capture the signal and variability of Hg cycling in this ecosystem, we increased the spatial and temporal resolution of the sampling regimes to measure process heterogeneity and identify areas of Hg hotspots (i.e., areas with elevated Hg concentrations) caused by soil Hg migration. Techniques of stable Hg isotopes were utilized to improve the knowledge of the Hg biogeochemical cycles in karst forests.[7,16,19,22−24] There are three unique dimensions of Hg isotopic fractionation, i.e., the mass dependent fractionation (MDF, mainly represented by $\delta^{202}Hg$), odd mass independent fractionation (odd-MIF, reported as $\Delta^{199}Hg$ and $\Delta^{201}Hg$), and even mass independent fractionation (even-MIF, reported as $\Delta^{200}Hg$ and $\Delta^{204}Hg$). The isotopic fractionation signals had been successfully applied for distinguishing the Hg sources and transport pathways of Hg biogeochemical processes in forest ecosystems,[25−28] since Hg source endmembers (e.g., Hg in rainfall, air, geological

Received: July 11, 2023
Revised: October 13, 2023
Accepted: October 16, 2023
Published: November 1, 2023

ACS Publications

© 2023 American Chemical Society

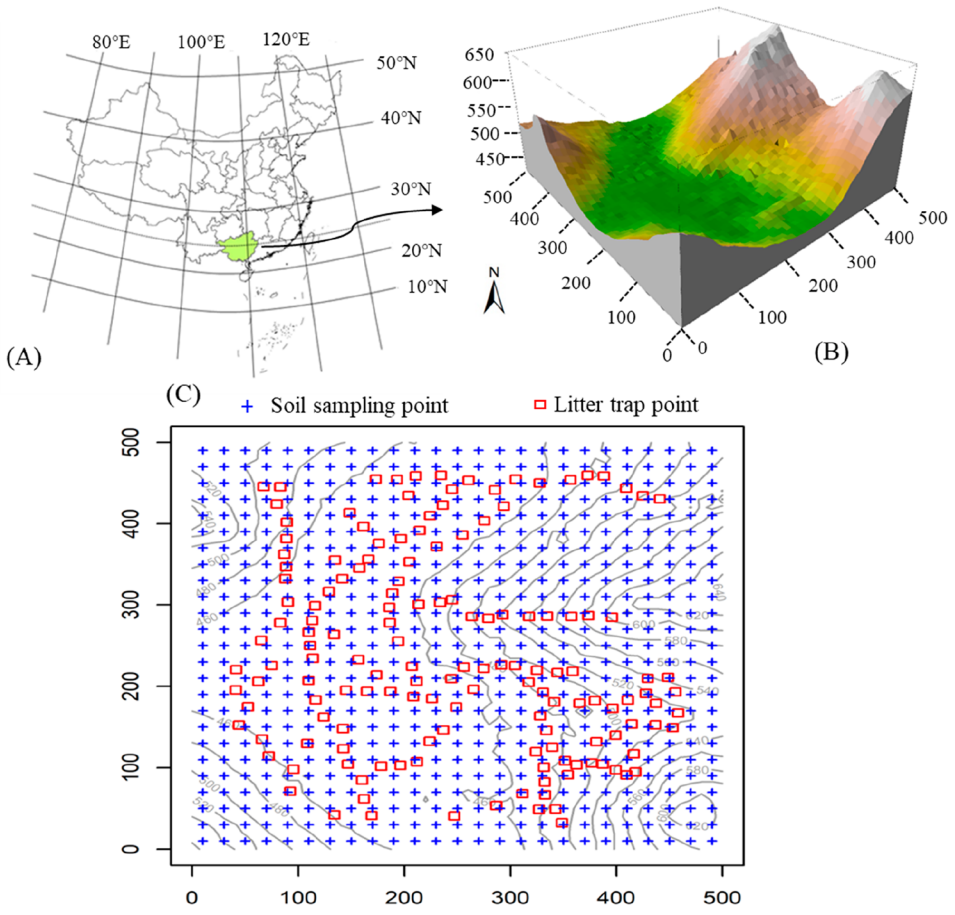

Figure 1. Description of the 25 ha studied karst forest watershed. (A) Site location and (B) topographical map (unit: m) and (C) sampling point locations (unit: m).

storages, and etc.) show unique Hg isotopic signatures.[9,29] Coupled with mass-balance models, these signals quantitatively resolve the contributing sources and associated transformation processes of Hg in forest ecosystems.

The objective of this work is to understand the spatial variation of atmospheric Hg deposition, soil Hg sources, and migration and accumulation processes of deposited Hg in the karst forest. We selected a 500 × 500 m karst forest watershed and applied the high-resolution sampling methodology and Hg isotopic signatures to trace the Hg sources and postdepositional processes. Implications for Hg accumulation and induced ecological risks in the karst forest are discussed.

2. METHODS

2.1. Site Description. The study site is located in the Mulun National Nature Reserve (107°54′01″−108°05′51″ E, 25°07′01″−25°12′22″ N) of Guangxi Province, China. The Mulun National Natural Reserve covers an area of 10 829 ha and is characterized by a typical karst landscape including a series of steep hills separated by low-lying land, potholes, and underground streams. The reserve was established to protect the pristine subtropical mixed evergreen-deciduous broadleaf forest ecosystem that develops on the limestone substrate. The area has a subtropical monsoon climate with a mean annual temperature, precipitation, and relative humidity of 19.4 °C, 1500 mm, and 79%, respectively. The soil is calcareous lithosol (limestone soil), and the average rock exposure ratio is greater than 60%.[30,31] The high rock exposure ratio leads to high heterogeneities of landcovers and soil layers. The traditional sampling regime of randomly collecting several (e.g., 5−7) soil samples cannot support comprehensively quantifying the atmospheric Hg depositions and soil Hg accumulation and migration in this karst forest ecosystem.

Our earlier studies have documented the sampling protocols extensively.[30,31] Briefly, we set a 25 ha (500 × 500 m) forest plot with elevations ranging from 442.6 to 651.4 m above sea level and slopes varying from 0 to 67°. The 25 ha plot is characterized by the rugged terrain of low-lying lands and steep hills. This sampling plot can represent the landform of the Mulun National Natural Reserve. Based on a recent vegetation survey, a total of 108 667 plants of 227 species, 147 genera, and 61 families were recorded. Evergreen woody species make up 62.5% of all of the species in the plot. *Cryptocarya microcarpa*, *Itoa orientalis*, *Platycarya longipes*, *Lindera communis*, and *Clausena dunniana* dominate the forest communities.[32]

2.2. Sampling Collection and Pretreatment. The 25 ha sampling plot was subdivided into 625 subplots (i.e., at the resolution of 20 × 20 m) for collecting surface soil samples (0−10 cm depth). At each sampling subplot, five subsamples were collected by a steel auger drill (5 cm diameter) within a radius of 1 m around the sample point and then mixed into one composite sample to represent average properties of the sampling point. We also sampled four deep rock samples in the elevation range of subplots. For litterfall collection, we set 151 litterfall traps placed in the 25 ha plot based on the terrain and community features (Figure 1). Each trap covered a 0.5 m^2

https://doi.org/10.1021/acs.est.3c05409
Environ. Sci. Technol. 2023, 57, 17490−17500

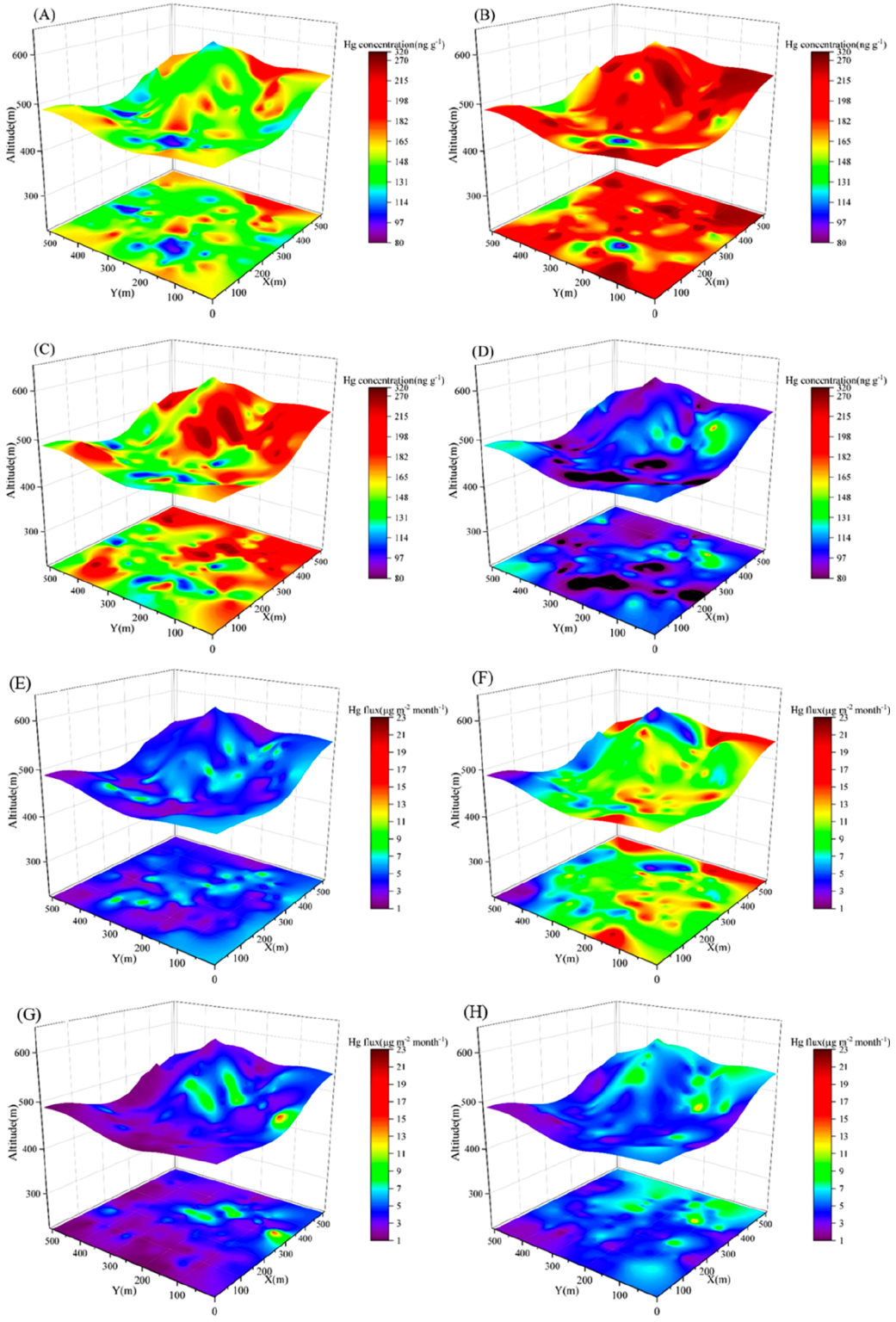

Figure 2. Temporospatial variation of litterfall Hg concentration and deposition in a 500 × 500 m karst forest plot. (A) shows Hg concentration in winter month (February); (B) shows Hg concentration in spring month (April); (C) shows Hg concentration in summer month (June); (D) shows Hg concentration in autumn month (September); (E) shows Hg flux in winter month (February); (F) shows Hg flux in spring month (April); (G) shows Hg flux in summer month (June); and (H) shows Hg flux in autumn month (September). In each subplot, the upper figure is the 3D spatial distribution, and the lower figure is the 2D spatial distribution through the projection drawing of 3D distribution.

area and was 0.5 m above ground. Litterfall samples were collected monthly from December 2020 to November 2021.

All samples were transported to the laboratory with soil samples air-dried at room temperature and litterfall oven-dried for 48 h at 50 °C to a constant weight. Our earlier works had shown that the oven-dried process would not lead to Hg loss in vegetation samples (<1%).[29,33] The dried samples were ground and sieved with a 200-mesh (74 μm) sieve, and the fraction

https://doi.org/10.1021/acs.est.3c05409
Environ. Sci. Technol. 2023, 57, 17490−17500

passed through the sieve was placed in metal-free plastic bags for chemical analysis.

2.3. Chemical Analysis. The chemical analysis of Hg concentration and isotopic compositions in vegetation and soil samples and the associated quality assurance/quality control (QA/QC) have been described in our earlier studies.[7,11,29,34−36] Briefly, Hg concentrations were measured by using a DMA-80 Hg analyzer. We determined the Hg concentration of one certified soil reference material and one parallel sample in every nine samples. The National Standard Reference Materials (SRM) of China GBW07405 (GSS-5, soil, Hg = 290 ± 40 ng g^{-1}) and GBW10020 (GSB-11, vegetation, Hg = 150 ± 25 ng g^{-1}) were used for QA/QC with a recovery of 95−105%. The bias of the parallel sample was less than 5%. We also measured soil organic carbon (SOC), copper (Cu), iron (Fe), and manganese (Mn) of surface soil samples. Detailed information can be found in the SI (Supporting Information).

Given the tempospatial distribution of litterfall Hg and surface soil Hg concentrations, we selected 28 litter samples, 35 surface soil samples, and 4 rock samples to determine Hg isotopic compositions (Figures S1−S2). For measurements of Hg isotopic composition, Hg in sample was preconcentrated by double-stage heating pyrolysis in a tube muffle furnace. The pure oxygen gas flow was set to 25−30 mL min^{-1} for sample combustion. The temperature programming of the first combustion furnace was carried out for soil and litter samples with a temperature increase of 10 °C min^{-1} for temperature ranges of 25−250 and 650−950 °C and 2.5 °C min^{-1} for 250−650 °C and finally was maintained at 950 °C for half an hour. The temperature of the second combustion furnace was maintained at 950 °C during the whole procedure. The Hg vapor from the sample was then captured using 5 mL of 40% reverse aqua regia ($HCl:HNO_3$ = 1:3, v/v) trapping solution.[37] The Hg concentration enriched in the trapping solution was measured by Tekran 2500 following US-EPA Method 1631. The preconcentration recovery was in the range of 91−106%. The Hg isotopic compositions were determined by a multicollector inductively coupled plasma mass spectrometer (MC-ICP-MS, Nu-Plasma II, Thermo Scientific). According to Bergquist and Blum,[38] the Hg MDF is reported as

$$\delta^{202}\mathrm{Hg}(‰) = 1000 \times [(^{202}\mathrm{Hg}/^{198}\mathrm{Hg}_{\mathrm{sample}})/(^{202}\mathrm{Hg}/^{198}\mathrm{Hg}_{\mathrm{NIST-3133}}) - 1] \quad (1)$$

where $(^{202}\mathrm{Hg}/^{198}\mathrm{Hg}_{\mathrm{NIST\text{-}3133}})$ represents the isotopic ratio in the standard sample (NIST-3133). MIF is calculated as

$$\Delta^{199}\mathrm{Hg}(‰) = \delta^{199}\mathrm{Hg} - 0.2520 \times \delta^{202}\mathrm{Hg} \quad (2)$$

$$\Delta^{200}\mathrm{Hg}(‰) = \delta^{200}\mathrm{Hg} - 0.5024 \times \delta^{202}\mathrm{Hg} \quad (3)$$

$$\Delta^{201}\mathrm{Hg}(‰) = \delta^{201}\mathrm{Hg} - 0.7520 \times \delta^{202}\mathrm{Hg} \quad (4)$$

To evaluate whether isotopic composition bias occurs during the preconcentration, we determined the Hg isotopic compositions of BCR-482 (vegetation SRM) and GSS-4 (soil SRM) in every 10 samples. The Hg isotopic signatures of BCR-482 were measured as δ^{202}Hg = −1.66 ± 0.11‰, Δ^{199}Hg = −0.56 ± 0.08‰, Δ^{200}Hg = −0.01 ± 0.04‰, and Δ^{201}Hg = −0.58 ± 0.08‰ (mean ± 2σ, n = 5), and those of GSS-4 were measured as δ^{202}Hg = −1.70 ± 0.16‰, Δ^{199}Hg = −0.34 ± 0.06‰, Δ^{201}Hg = −0.34 ± 0.06‰, and Δ^{200}Hg = −0.00 ± 0.04‰ (mean ± 2σ, n = 5). The NIST-8610 was analyzed for every 10 samples during Hg isotope measurements, with δ^{202}Hg = −0.54 ± 0.08‰, Δ^{199}Hg = −0.00 ± 0.06‰, Δ^{200}Hg = 0.00 ± 0.03‰, and Δ^{201}Hg = −0.03 ± 0.05‰ (mean ± 2σ, n = 9). All measured Hg isotopic signatures of SRM were consistent with their recommended values.[39,40]

2.4. Data Analysis. IBM SPSS Statistics v26.0 was utilized for statistical analysis at the 95% confidence level. We used one-way ANOVA to determine significant differences of measured values when data were normally distributed. Otherwise, the Kruskal−Wallis test was applied. Pearson correlation analysis was applied to evaluate the relation among variables. Specifically, we analyzed the correlation between Hg isotopes and the topographic wetness index (TWI). TWI is commonly used to quantify terrain-driven variation in soil moisture. TWI was calculated as the ratio of the area upslope from any given point on the landscape to the local slope at that point as follows:

$$\mathrm{TWI} = \ln(a/\tan b) \quad (5)$$

where a is the upslope contributing area and b is the slope. We also construct a Hg isotope mixing model to quantify the Hg source contribution in surface soil. Our earlier studies have shown that the Hg isotope mixing model coupled with Monte Carlo simulations would effectively estimate the uncertainties of the model results.[8,11] These uncertainties were quantified by generating one million groups of MIF signatures randomly ranging from mean − 2SD (standard deviation) to mean + 2SD to solve the Hg isotope mixing model.

3. RESULTS

3.1. Tempospatial Distribution of Litter Hg Deposition. Figures 2 and S3 display the temporospatial distribution of the litterfall Hg concentration and flux. The annual average Hg concentration in litterfall was 143 ± 28 ng g^{-1}, leading to the total litterfall Hg deposition of 60.5 ± 12.9 μg m^{-2} $year^{-1}$. The litterfall Hg concentration exhibited a seasonal trend with the lowest concentration in autumn (109 ± 14 ng g^{-1}) and the highest Hg concentration in spring (185 ± 36 ng g^{-1}). The litterfall Hg deposition flux followed the same trend, at 8.2 ± 4.4 μg m^{-2} $month^{-1}$ in spring and 4.3 ± 1.6 μg m^{-2} $month^{-1}$ in autumn.

The litterfall Hg concentration showed a significant spatial heterogeneity in the 25 ha sampling plot. The hillslope points had elevated litterfall Hg concentration compared to low-lying land points (Figure 2A−D). Specifically, almost hillslope sampling points in spring (up to 90% of whole watershed) had Hg concentrations greater than 180 ng g^{-1} (i.e., about 2−3 times of observed Hg concentration in remote subtropical litterfall[9]), while low-lying lands had Hg concentration in the range of 80−100 ng g^{-1}. However, in autumn, there were few Hg sampling points with a Hg concentration more than 180 ng g^{-1} on the hillslope. In summer and winter, the number of sampling points with >180 ng g^{-1} Hg concentration on the hillslope fell between the values in autumn and in spring. Litterfall Hg deposition was controlled by litterfall biomass production (Figure S4) and Hg concentration. The hillslope samples had elevated Hg concentration yet low litterfall Hg deposition (Figure 2E−H).

3.2. Spatial Distribution of Surface Soil Hg Concentration. The surface soil Hg concentration showed large spatial heterogeneity, ranging from 42 to 828 ng g^{-1} with a mean of 399 ± 105 ng g^{-1}. Hg is greatly accumulated in

https://doi.org/10.1021/acs.est.3c05409
Environ. Sci. Technol. 2023, 57, 17490−17500

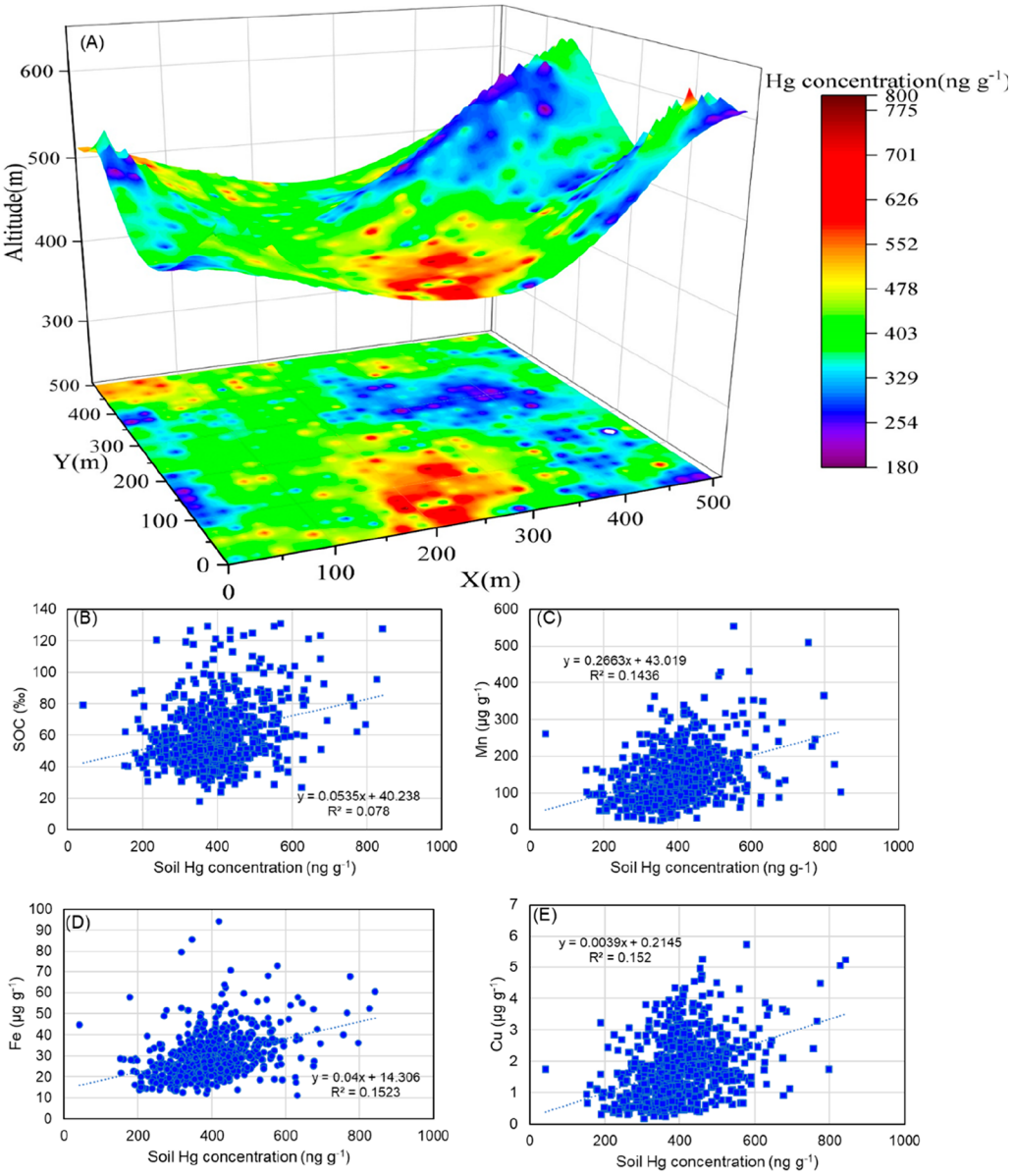

Figure 3. Spatial variation of surface soil Hg and correlations. (A) is for soil Hg concentration; (B) shows correlation between soil Hg concentration and SOC; (C) shows correlation between soil Hg concentration and Mn; (D) shows correlation between soil Hg concentration and Fe; (E) shows correlation between soil Hg concentration and Cu. In (A), the upper figure is the 3D spatial distribution, and the lower figure is the 2D spatial distribution through the projection drawing of 3D distribution.

surface soil compared to the values in deep rock, with a mean value of 3 ± 1 ng g^{-1} (n = 4). The Hg concentration in surface soil exhibited a spatial trend opposite to that of the litterfall Hg concentration (Figure 3A). The watershed of low-lying land showed high surface soil Hg but low litterfall concentration. Specifically, Hg was highly accumulated in the region of the watershed outlet (i.e, downstream drainage point, as the point on the surface at which water flows out of a watershed), with concentrations higher than 800 ng g^{-1} and nearly 5 times the Hg concentrations on the hillslope. In addition, the surface soil Hg concentration showed a significant correlation to Mn, Fe, and Cu concentrations (p < 0.001; Figure 3C−E) but did not correlate to the SOC (Figure 3B).

3.3. Hg Isotopic Signatures. Figure 4 shows the relationships among Hg isotopic compositions and with other measured parameters. The average δ^{202}Hg in litterfall was −2.95 ± 0.23‰, Δ^{199}Hg was −0.16 ± 0.04‰, and Δ^{200}Hg was −0.02 ± 0.03‰. The Hg isotopic signatures of litterfall did not show a distinct temporal trend (Figure S5). In surface soil, the average δ^{202}Hg was −2.17 ± 1.14‰, Δ^{199}Hg was −0.30 ± 0.18‰, and Δ^{200}Hg was −0.00 ± 0.03‰. The Hg isotopic signatures in rock showed −0.67 ± 0.37‰ of δ^{202}Hg, −0.14 ± 0.03‰ of Δ^{199}Hg, and −0.04 ± 0.03‰ of Δ^{200}Hg.

The Δ^{199}Hg values showed a strong anticorrelation to δ^{202}Hg in litterfall and surface soil samples, a significantly positive correlation to Δ^{200}Hg in surface soil, and a significantly negative correlation to Hg concentration in litter and surface soil (Figure 4A−C). The scattered plot of Δ^{199}Hg versus Δ^{201}Hg in litterfall and surface soil (Figure 4D) showed a slope of ∼1.0. Finally, δ^{202}Hg in litterfall and surface soil samples displayed the significantly positive correlations to Hg concentration and TWI (topographic wetness index; Figure 4E,F).

https://doi.org/10.1021/acs.est.3c05409
Environ. Sci. Technol. 2023, 57, 17490−17500

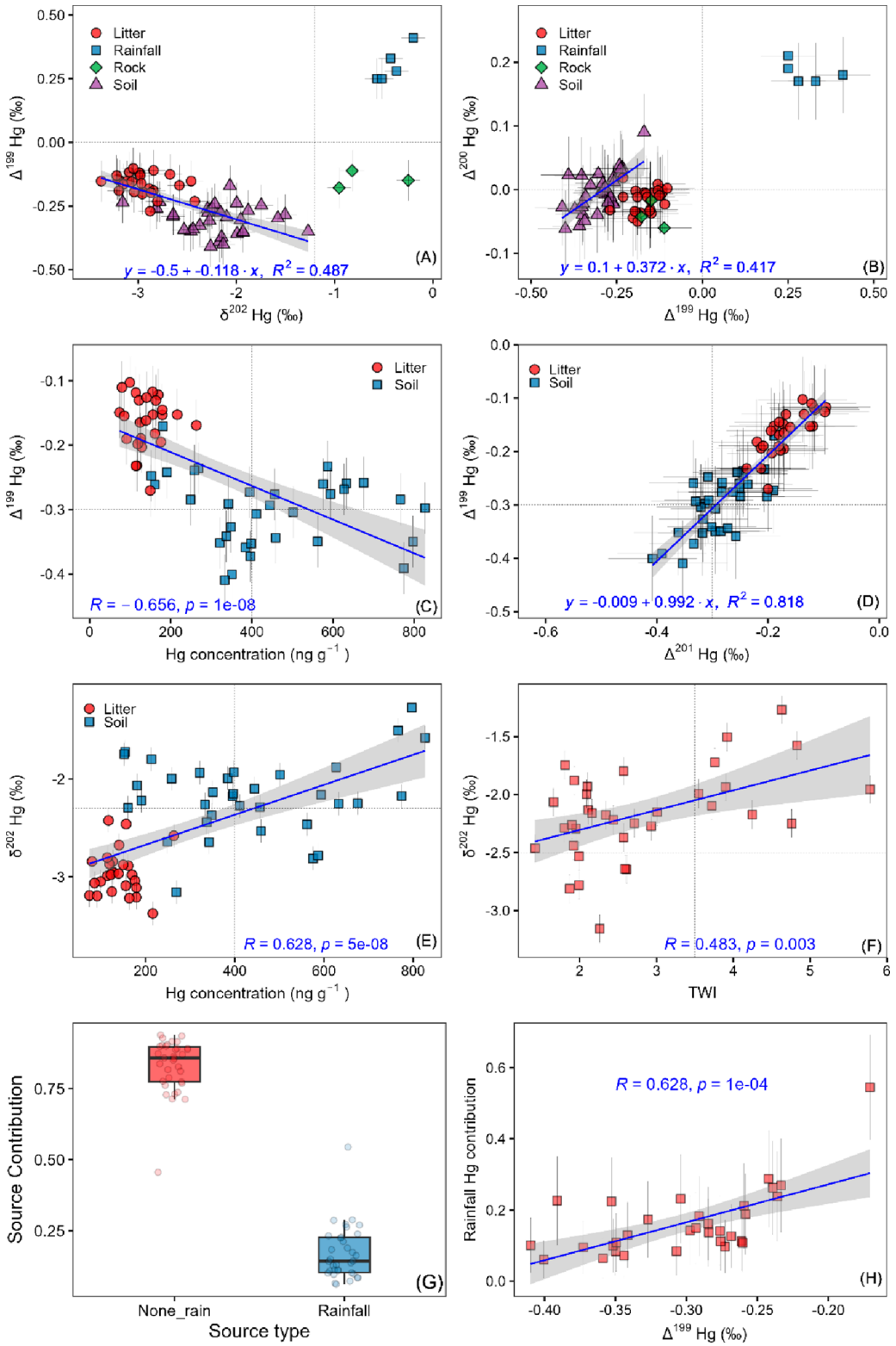

Figure 4. Correlations of Hg isotopic signatures: (A) Δ^{199}Hg versus δ^{202}Hg; (B) Δ^{200}Hg versus Δ^{199}Hg; (C) Δ^{199}Hg versus Hg concentration; (D) Δ^{199}Hg versus Δ^{201}Hg; (E) δ^{202}Hg versus Hg concentration; (F) δ^{202}Hg versus TWI (topographic wetness index); (G) source contribution; (H) rainfall Hg contribution versus Δ^{199}Hg. The error bars stand for 2σ. The Hg isotopic data of rainfall are obtained from previous measurements in another karst forest.[22]

4. DISCUSSION

4.1. Understanding Tempospatial Trends of Hg Accumulation in Litterfall. Hg in litterfall of remote subtropical regions has a concentration of 40−90 ng g^{-1}.[9,29,41] We observed that litterfall Hg concentrations in the studied karst forest are 1−2 times greater than those observed elsewhere, which leads to 1−2 times litterfall Hg fluxes compared to remote subtropical forests.[9,20,42] This is

https://doi.org/10.1021/acs.est.3c05409
Environ. Sci. Technol. 2023, 57, 17490−17500

likely due to that the karst forest watershed is 20−30 km away from several mining sites and therefore influenced by anthropogenic Hg emissions. The Hg isotopic signatures confirm this hypothesis. The litterfall in remote subtropical forests has a typical Δ^{199}Hg ranging from −0.4‰ to −0.2‰[29,42,43] but −0.16 ± 0.04‰ in this study. The close to zero Δ^{199}Hg signatures point to the contribution of anthropogenic sources[9,44], thus diluting the negative Δ^{199}Hg in background air.

There is a clear seasonal trend of litterfall Hg concentration. Spring has the highest Hg concentration, followed by summer and then autumn and winter (Figure 2A−D). Earlier field observations displayed that the seasonal trends of atmospheric Hg concentration in South China depend on trends of anthropogenic emissions and monsoon shifts and possibly higher atmospheric Hg concentrations in autumn and winter[45] due to the elevated anthropogenic Hg emissions and weaken monsoon.[46,47] The elevated litterfall Hg concentration observed in spring cannot be explained by the seasonal trend of the atmospheric Hg concentration.

The seasonal trend of litterfall Hg concentration is most likely caused by the seasonal vegetation types that exhibit varied atmospheric Hg^0 assimilation abilities. The karst watershed is a mixed forest plot with evergreen broadleaf (EB) and deciduous broadleaf (DB) tree species. The instantaneous air-foliage Hg exchange flux of EB foliage is comparable to the flux of common DB foliage.[29] However, the EB foliage has a 1 to 1.5 year lifespan, with the peak litterfall flux in spring, while DB foliage has a 6 to 8 month lifespan with peak litterfall flux in autumn and winter (Figure S4). A longer foliage lifespan increases the quantity of atmospheric Hg^0 uptake,[3,9,29] thus leading to the elevated Hg concentration in spring EB litterfall. The nearly double Hg concentration in spring compared to in autumn (185 ± 36 ng g^{-1} versus 109 ± 14 ng g^{-1}) is consistent with double foliage lifespan of EB in contrast to DB tree species.

We observed the higher Hg concentration in litterfall mainly scattering on the hillslope in each season. Such elevated Hg concentrations on the hillslope can be attributed to several causes. One is that topographical variations induced elevated atmospheric Hg on the hillslope. The prevailing wind direction in warming seasons is from south to north (i.e., East Asian monsoon) and in cold seasons is from north to south (i.e., winter monsoon). The southeastern−northwestern trending of hillslopes in the karst watershed can partially block the air mass transportation to reduce Hg accumulation in the air of low-lying land areas. This topographical impact is obvious in spring, since litterfall in this season is only derived from EB tree species, thus without different vegetation influences. The prevailing wind in spring also likely is related to elevated atmospheric Hg^0 concentration in southwestern China.[48,49] Therefore, most sampling points on the hillslope in spring have a litterfall Hg concentration greater than 180 ng g^{-1}.

The spatial distribution of EB and DB tree species also has an effect on the observed spatial trend of litterfall Hg in summer, autumn, and winter seasons. The low-lying land has predominant EB tree species, compared to predominant DB over the hillslope (Figure S6). The DB litterfall occurs predominantly in the autumn and winter. As previously discussed, the DB litterfall has a lower Hg concentration in contrast to the EB litterfall. The higher biomass production of DB litterfall on the hillslope can partially offset differences in litterfall Hg deposition between the low-lying land and hillslope in these seasons.

The spatial variation of tree physiological processes that control foliage uptake of atmospheric Hg^0 and its subsequent accumulation and translocation also have an impact on the spatial distribution of litterfall Hg concentrations. Our earlier study showed that the tree species competitive regime (i.e., tree species response manifested when two or more individuals' demand for resources exceeds resource supplies) could cause different atmospheric Hg^0 uptake on the canopy layers.[50] In this study, we found that the Shannon and Simpson index (i.e., a measure of vegetation diversity, a greater value means higher diversity of tree species) is significantly correlated to the litterfall Hg concentration in each season (Figure S7). This can be explained by trees growing in a competitive environment tending to maximize the efficiency of light and water use to assimilate and transport nutrients, thus influencing atmospheric Hg^0 uptake rate.[50]

The observed Hg isotopic compositions showed insignificant tempospatial trends (R^2 = 0.05 between Δ^{199}Hg and slope; Figure S5). This can be explained by two causes. One is the relatively small range of Δ^{199}Hg of atmospheric Hg^0,[35,44] thus leading to the Δ^{199}Hg being unable to distinguish the fine resolution of atmospheric Hg^0 variations in the watershed. Another potential explanation is that the complicated disturbances of anthropogenic, topographical, and monsoon variations lead to the insignificant tempospatial trends of atmospheric Hg isotopic compositions. We recommend further studies to verify these issues, specifically the spatiotemporal variations of isotopic signatures of atmospheric Hg^0.

4.2. Quantifying Hg Sources and Postdepositional Processes in Surface Soil. Three source endmembers have been identified for soil Hg accumulation in forest, including atmospheric Hg^{2+} deposition, atmospheric Hg^0 deposition, and geogenic sources. Hg^{2+} in precipitation exhibits negative MDF as well as positive odd-MIF and even-MIF signals.[16,51−53] Atmospheric Hg^0 in remote regions shows slightly negative odd-MIF, negative even-MIF, and small MDF signatures.[15,54−56] Geogenic Hg sources feature negative MDF and negligible odd-MIF and even-MIF signals.[33,57] Most Hg biogeochemical processes in the forest soil can induce MDF, while only several Hg redox processes can induce odd-MIF.[9,44] The soil Hg^0 emission processes usually lead to the heavier Hg isotopes accumulated in soil, i.e., +MDF in soil Hg.[19,58,59] Dark oxidation or reduction of soil organic matter is usually associated with a small negative odd-MIF in soil.[15,60] Photoreduction of soil Hg bounded by S-containing organic ligands leads to a relatively large positive odd-MIF in the product Hg^0.[61,62] Therefore, we used the MIF signatures to trace Hg sources and processes in the surface soil.

The negative Δ^{199}Hg signatures (Figure 4A) and the significantly negative correlation between Hg concentration and Δ^{199}Hg in litterfall and surface soil (Figure 4C) suggest that vegetation uptake of atmospheric Hg^0 contributes to Hg accumulation in surface soil. However, Δ^{199}Hg signatures of surface soil show −0.2 to −0.1‰ more shift than signatures of litterfall, indicating that the Hg postdepositional processes have altered the odd-MIF. The Δ^{199}Hg signatures cannot be directly used to quantify the contribution of the atmospheric Hg sources. Since known Hg biogeochemical processes in forests do not shift Δ^{200}Hg,[9,63] Δ^{200}Hg is a superior tracer to identify the atmospheric Hg^{2+} deposition sources. Therefore, Δ^{200}Hg signals were utilized for estimating the contribution of rainfall

https://doi.org/10.1021/acs.est.3c05409
Environ. Sci. Technol. 2023, 57, 17490−17500

inputs (i.e., atmospheric Hg^{2+}) and nonrainfall inputs as following:

$$\Delta^{200}Hg_{rainfall} \times f_{rainfall} + \Delta^{200}Hg_{nonrainfall} \times (1 - f_{rainfall}) = \Delta^{200}Hg_{soil} \quad (6)$$

where $\Delta^{200}Hg_{rainfall}$ is the signature of atmospheric Hg^{2+} inputs and obtained from an observation in another karst forest;[22] $f_{rainfall}$ is the atmospheric Hg^{2+} input contribution. The $\Delta^{200}Hg$ signatures of rock and litterfall are comparable and both with a mean of $-0.03 \pm 0.03‰$. Thus, we set $\Delta^{200}Hg_{nonrainfall} = -0.03 \pm 0.03‰$ in this study.

Earlier studies have depicted 10−25% contribution of atmospheric Hg^{2+} input to forest soil.[8,9,15,43,64] The result of the Hg isotope mixing model is similar to an average of 17 ± 10% of atmospheric Hg^{2+} input (Figure 4G), which increases with the increasing $\Delta^{199}Hg$ signatures in surface soil (Figure 4H). This is consistent with the significantly positive correlation between $\Delta^{199}Hg$ and $\Delta^{200}Hg$, as shown in Figure 4B.

The positive $\delta^{202}Hg$ values and much lower Hg concentration in rock (10−100 times lower) than in surface soil suggest that the contribution of the geogenic source can be ignored. There are two main pathways of deposited atmospheric Hg^0: litterfall Hg deposition and direct atmospheric Hg^0 deposition to organic soil. Given the strongly negative correlation between $\delta^{202}Hg$ and $\Delta^{199}Hg$ in litterfall and surface soil (Figure 4A), litterfall Hg deposition appears to be more important in contributing to Hg accumulation in forest soil. We further estimated the postdepositional processes induced an odd-MIF shift by

$$\Delta^{199}Hg_{shift} = \Delta^{199}Hg_{rainfall} \times f_{rainfall} + \Delta^{199}Hg_{litterfall} \times (1 - f_{rainfall}) - \Delta^{199}Hg_{soil} \quad (7)$$

The estimated $\Delta^{199}Hg_{shift}$ ranges from 0.1 to 0.3‰ in Figure S8. There are two reduction processes inducing positive odd-MIF in the product of Hg^0. One is photochemical reduction of Hg^{2+} complexed to S-containing organic ligands, and another is dark reduction of Hg^{2+} by organic matter.[9,44] The photochemical reduction of Hg^{2+} complexed to S-containing organic ligands is usually associated with the larger $\varepsilon^{odd\text{-}MIF}Hg_{product\text{-}reactant}$ (i.e., odd-MIF enrichment factor between the product and reactant) than dark reduction of Hg^{2+} by organic matter ($\varepsilon^{MIF}Hg_{product\text{-}reactant}$: 1.03 versus 0.17−0.26).[60,61] Additionally, the intensive canopy shading limits Hg photoreduction, while the elevated SOC (4−12% in this study) in surface soil promotes soil organic matter (SOM) induced dark reduction.[9,44] The observed 0.1−0.3‰ of $\Delta^{199}Hg_{shift}$ is most likely caused by an SOM-induced dark reduction, which has also been observed in boreal and subtropical forests.[15,19] SOM-induced dark reduction is usually associated with a slope of 1.5−1.7 for $\Delta^{199}Hg/\Delta^{201}Hg$.[60,62] In this work, the slope is 1.0 (Figure 4D). This is because the extent of this SOM-induced dark reduction is less than 50% based on the estimation of Rayleigh fractionation model,[15,50] and the small distribution of $\Delta^{199}Hg$ in surface soil would induce a large uncertainty for the calculation of $\Delta^{199}Hg$ versus $\Delta^{201}Hg$ slope.

4.3. Hg Migration in Surface Soil. The spatial distribution of litterfall Hg shows the opposite trend of the spatial distributions of surface soil Hg. The surface soil in the low-lying land of the watershed shows comparatively higher Hg concentrations (Figure 3A). Since SOC mainly comes from decomposed litterfall and the surface soil Hg shows a weak correlation with SOC (Figure 3B), litterfall Hg deposition cannot explain the spatial trend of the surface soil Hg concentration. Direct atmospheric Hg^0 deposition and the subsequent oxidation on SOM also induce a small odd-MIF shift (<0.3‰).[65] However, the estimated $\Delta^{199}Hg_{shift}$ shows an insignificant correlation to the surface Hg concentration (Figure S8). This suggests that the elevated level of Hg accumulation in the low-lying land was not caused by direct atmospheric Hg^0 deposition in these regions.

Given the high erosion rate of fragmented carbonate rock in the karst region, we examined the influence of soil erosion on shaping the spatial trend of the surface soil Hg concentration. The distribution of elevated Hg concentration coincided with the water flow direction. The most concentrated Hg accumulation in the outlet region of the watershed is where the surface soil has a 400-times greater concentration of Hg than in rock (Figure 3A). This suggests distinct Hg migration through soil erosion. This can be further supported by several evidences. There is an increase in soil $\delta^{202}Hg$ signatures with increasing TWI (Figure 4F). The higher TWI represents a greater ability to accumulate water and to intercept the sediment of upland runoff. The legacy Hg with the heavier isotope[43,59] tends to be absorbed to organic compounds in fine soil particles[66−70] and transported and accumulated in the low-lying land with the high TWI. Additionally, we observed the elevated SOC contents (ranging 8−13% in Figure S9) in the downstream drainage point with the highest TWI. During the soil erosion and sedimentation processes, the soil minerals also likely play a role in enhancing Hg accumulation. At the mineral−organic matter interface, Fe oxides and Mn oxides can adsorb organometal complexes at the particle−water interface.[71,72] This is supported by the significant correlations among Fe, Mn, Cu, and Hg in surface soil (Figure 3C−E).

5. IMPLICATIONS

In nonkarst forests, Hg efflux via soil erosion and runoff accounts for less than 5% of total Hg inputs,[9,73,74] except during the deforestation that causes a pulse of soil Hg erosion.[9,75,76] In this study, the high soil erosion resulting in the unusually high Hg accumulation in the low-lying land of the karst forest watershed is highlighted. The surface soil Hg concentration in the low-lying land is 4−10 times higher than the values observed in most remote/rural forest soil.[9,34] Hg transported through soil erosion increases the Hg burden to the downstream aquatic ecosystems where inorganic Hg can be transformed into highly toxic methylated Hg and then bioaccumulated and biomagnified via food chains.[77−79] In addition, the high connectivity of ground and underground water flow in the karst forest[12−14] also promotes soil Hg leaching into the groundwater and increases the risk of groundwater Hg pollution. Using the Hg isotopic tracing techniques, an earlier study has shown that Hg in groundwater was derived from the surface soil Hg leaching.[22] We recommend further assessing the ecological risks caused by soil Hg migration in the karst forest watershed.

■ ASSOCIATED CONTENT

Supporting Information

The Supporting Information is available free of charge at https://pubs.acs.org/doi/10.1021/acs.est.3c05409.

https://doi.org/10.1021/acs.est.3c05409
Environ. Sci. Technol. 2023, 57, 17490−17500

Additional data for Hg signatures in Table S1. Additional figures as mentioned in the text in Figures S1−S9 (PDF)

AUTHOR INFORMATION

Corresponding Author

Xun Wang − *State Key Laboratory of Environmental Geochemistry, Institute of Geochemistry, Chinese Academy of Sciences, Guiyang 550081, China;* orcid.org/0000-0002-7407-8965; Email: wangxun@mail.gyig.ac.cn

Authors

Hu Du − *Key Laboratory of Agro-Ecological Processes in Subtropical Region, Institute of Subtropical Agriculture, Chinese Academy of Sciences, Changsha 410125 Hunan, China; Huanjiang Observation and Research Station for Karst Ecosystems, Institute of Subtropical Agriculture, Chinese Academy of Sciences, Huanjiang 547100 Guangxi, China*

Wei Yuan − *State Key Laboratory of Environmental Geochemistry, Institute of Geochemistry, Chinese Academy of Sciences, Guiyang 550081, China;* orcid.org/0000-0003-3329-2081

Fei Wu − *State Key Laboratory of Environmental Geochemistry, Institute of Geochemistry, Chinese Academy of Sciences, Guiyang 550081, China*

Longyu Jia − *State Key Laboratory of Environmental Geochemistry, Institute of Geochemistry, Chinese Academy of Sciences, Guiyang 550081, China*

Nantao Liu − *State Key Laboratory of Environmental Geochemistry, Institute of Geochemistry, Chinese Academy of Sciences, Guiyang 550081, China*

Che-Jen Lin − *Center for Advances in Water and Air Quality, Lamar University, Beaumont, Texas 77710, United States*

Jiang Gan − *Key Laboratory of Agro-Ecological Processes in Subtropical Region, Institute of Subtropical Agriculture, Chinese Academy of Sciences, Changsha 410125 Hunan, China; Huanjiang Observation and Research Station for Karst Ecosystems, Institute of Subtropical Agriculture, Chinese Academy of Sciences, Huanjiang 547100 Guangxi, China*

Fuping Zeng − *Key Laboratory of Agro-Ecological Processes in Subtropical Region, Institute of Subtropical Agriculture, Chinese Academy of Sciences, Changsha 410125 Hunan, China; Huanjiang Observation and Research Station for Karst Ecosystems, Institute of Subtropical Agriculture, Chinese Academy of Sciences, Huanjiang 547100 Guangxi, China*

Kelin Wang − *Key Laboratory of Agro-Ecological Processes in Subtropical Region, Institute of Subtropical Agriculture, Chinese Academy of Sciences, Changsha 410125 Hunan, China; Huanjiang Observation and Research Station for Karst Ecosystems, Institute of Subtropical Agriculture, Chinese Academy of Sciences, Huanjiang 547100 Guangxi, China*

Xinbin Feng − *State Key Laboratory of Environmental Geochemistry, Institute of Geochemistry, Chinese Academy of Sciences, Guiyang 550081, China;* orcid.org/0000-0002-7462-8998

Complete contact information is available at: https://pubs.acs.org/10.1021/acs.est.3c05409

Notes

The authors declare no competing financial interest.

ACKNOWLEDGMENTS

This work was funded by National Natural Science Foundation of China (42122053, 42071073), National Key Research and Development Program of China (2022YFF1300703), Youth Innovation Promotion Association of the Chinese Academy of Sciences (2021366), Natural Science Foundation of Guangxi Province (2023GXNSFAA026109).

REFERENCES

(1) UN-Environment. *Global Mercury Assessment 2018*; UN-Environment Programme, Chemicals and Health Branch, 2019.

(2) Selin, N. E. Global Biogeochemical Cycling of Mercury: A Review. *Annual Review of Environment and Resources* **2009**, *34* (1), 43−63.

(3) Wang, X.; Bao, Z.; Lin, C.-J.; Yuan, W.; Feng, X. Assessment of Global Mercury Deposition through Litterfall. *Environ. Sci. Technol.* **2016**, *50* (16), 8548−8557.

(4) Lindberg, S.; Bullock, R.; Ebinghaus, R.; Engstrom, D.; Feng, X.; Fitzgerald, W.; Pirrone, N.; Prestbo, E.; Seigneur, C. A Synthesis of Progress and Uncertainties in Attributing the Sources of Mercury in Deposition. *Ambio* **2007**, *36* (1), 19−33.

(5) Obrist, D.; Kirk, J. L.; Zhang, L.; Sunderland, E. M.; Jiskra, M.; Selin, N. E. A review of global environmental mercury processes in response to human and natural perturbations: Changes of emissions, climate, and land use. *Ambio* **2018**, *47* (2), 116−140.

(6) Wang, B.; Yuan, W.; Wang, X.; Li, K.; Lin, C. J.; Li, P.; Lu, Z.; Feng, X.; Sommar, J. Canopy-Level Flux and Vertical Gradients of Hg(0) Stable Isotopes in Remote Evergreen Broadleaf Forest Show Year-Around Net Hg(0) Deposition. *Environ. Sci. Technol.* **2022**, *56* (9), 5950−5959.

(7) Wang, X.; Luo, J.; Yin, R.; Yuan, W.; Lin, C. J.; Sommar, J.; Feng, X.; Wang, H.; Lin, C. Using Mercury Isotopes To Understand Mercury Accumulation in the Montane Forest Floor of the Eastern Tibetan Plateau. *Environ. Sci. Technol.* **2017**, *51* (2), 801−809.

(8) Wang, X.; Luo, J.; Yuan, W.; Lin, C. J.; Wang, F.; Liu, C.; Wang, G.; Feng, X. Global warming accelerates uptake of atmospheric mercury in regions experiencing glacier retreat. *Proc. Natl. Acad. Sci. U. S. A.* **2020**, *117* (4), 2049−2055.

(9) Wang, X.; Yuan, W.; Lin, C.-J.; Feng, X. Mercury cycling and isotopic fractionation in global forests. *Crit Rev. Env Sci. Tec* **2022**, *52* (21), 3763−3786.

(10) Obrist, D.; Agnan, Y.; Jiskra, M.; Olson, C. L.; Colegrove, D. P.; Hueber, J.; Moore, C. W.; Sonke, J. E.; Helmig, D. Tundra uptake of atmospheric elemental mercury drives Arctic mercury pollution. *Nature* **2017**, *547* (7662), 201−204.

(11) Wang, X.; Yuan, W.; Lin, C. J.; Luo, J.; Wang, F.; Feng, X.; Fu, X.; Liu, C. Underestimated Sink of Atmospheric Mercury in a Deglaciated Forest Chronosequence. *Environ. Sci. Technol.* **2020**, *54* (13), 8083−8093.

(12) Jiang, Z.; Lian, Y.; Qin, X. Rocky desertification in Southwest China: Impacts, causes, and restoration. *Earth-Sci. Rev.* **2014**, *132*, 1−12.

(13) Vilhar, U.; Kermavnar, J.; Kozamernik, E.; Petrič, M.; Ravbar, N. The effects of large-scale forest disturbances on hydrology - An overview with special emphasis on karst aquifer systems. *Earth-Sci. Rev.* **2022**, *235*, 104243.

(14) Xu, X.; Yan, Y.; Dai, Q.; Yi, X.; Hu, Z.; Cen, L. Spatial and temporal dynamics of rainfall erosivity in the karst region of southwest China: Interannual and seasonal changes. *Catena* **2023**, *221*, 106763.

(15) Jiskra, M.; Wiederhold, J. G.; Skyllberg, U.; Kronberg, R. M.; Hajdas, I.; Kretzschmar, R. Mercury deposition and re-emission pathways in boreal forest soils investigated with Hg isotope signatures. *Environ. Sci. Technol.* **2015**, *49* (12), 7188−7196.

(16) Demers, J. D.; Blum, J. D.; Zak, D. R. Mercury isotopes in a forested ecosystem: Implications for air-surface exchange dynamics

and the global mercury cycle. *Global Biogeochem Cy* **2013**, *27* (1), 222−238.
(17) Lindberg, S. E.; Price, J. L. Airborne Emissions of Mercury from Municipal Landfill Operations: A Short-Term Measurement Study in Florida. *J. Air Waste Manag Assoc* **1999**, *49* (5), 520−532.
(18) Lindberg, S. E.; Hanson, P. J.; Meyers, T. P.; Kim, K. H. Air/surface exchange of mercury vapor over forests - The need for a reassessment of continental biogenic emissions. *Atmos. Environ.* **1998**, *32* (5), 895−908.
(19) Yuan, W.; Wang, X.; Lin, C. J.; Sommar, J. O.; Wang, B.; Lu, Z.; Feng, X. Quantification of Atmospheric Mercury Deposition to and Legacy Re-emission from a Subtropical Forest Floor by Mercury Isotopes. *Environ. Sci. Technol.* **2021**, *55* (18), 12352−12361.
(20) Yuan, W.; Wang, X.; Lin, C. J.; Zhang, H.; Feng, X.; Lu, Z. Impacts of Extreme Weather on Mercury Uptake and Storage in Subtropical Forest Ecosystems. *Journal of Geophysical Research: Biogeosciences* **2022**, *127* (1), 10.1029/2021JG006681.
(21) Li, Z. W.; Xu, X. L.; Wang, K. L. Effects of distribution patterns of karst landscapes on runoff and sediment yield in karst watersheds. *Catena* **2023**, *223*, 106947.
(22) Xia, J.; Wang, J.; Zhang, L.; Wang, X.; Yuan, W.; Peng, T.; Zheng, L.; Tian, W.; Feng, X. Migration and transformation of soil mercury in a karst region of southwest China: Implications for groundwater contamination. *Water Res.* **2022**, *226*, 119271.
(23) Yuan, W.; Wang, X.; Lin, C. J.; Wu, F.; Luo, K.; Zhang, H.; Lu, Z.; Feng, X. Mercury Uptake, Accumulation, and Translocation in Roots of Subtropical Forest: Implications of Global Mercury Budget. *Environ. Sci. Technol.* **2022**, *56* (19), 14154−14165.
(24) Zheng, W.; Obrist, D.; Weis, D.; Bergquist, B. A. Mercury isotope compositions across North American forests. *Global Biogeochemical Cycles* **2016**, *30* (10), 1475−1492.
(25) Kritee, K.; Blum, J. D.; Barkay, T. Mercury stable isotope fractionation during reduction of Hg(II) by different microbial pathways. *Environ. Sci. Technol.* **2008**, *42* (24), 9171−9177.
(26) Kritee, K.; Blum, J. D.; Johnson, M. W.; Bergquist, B. A.; Barkay, T. Mercury stable isotope fractionation during reduction of Hg(II) to Hg(0) by mercury resistant microorganisms. *Environ. Sci. Technol.* **2007**, *41* (6), 1889−1895.
(27) Zheng, W.; Hintelmann, H. Isotope fractionation of mercury during its photochemical reduction by low-molecular-weight organic compounds. *J. Phys. Chem. A* **2010**, *114* (12), 4246−4253.
(28) Zheng, W.; Hintelmann, H. Nuclear field shift effect in isotope fractionation of mercury during abiotic reduction in the absence of light. *J. Phys. Chem. A* **2010**, *114* (12), 4238−4245.
(29) Yuan, W.; Sommar, J.; Lin, C.-J.; Wang, X.; Li, K.; Liu, Y.; Zhang, H.; Lu, Z.; Wu, C.; Feng, X. Stable Isotope Evidence Shows Re-emission of Elemental Mercury Vapor Occurring after Reductive Loss from Foliage. *Environ. Sci. Technol.* **2019**, *53* (2), 651−660.
(30) Du, H.; Hu, F.; Zeng, F. P.; Wang, K. L.; Peng, W. X.; Zhang, H.; Zeng, Z. X.; Zhang, F.; Song, T. Q. Spatial distribution of tree species in evergreen-deciduous broadleaf karst forests in southwest China. *Sci. Rep.* **2017**, *7* (1), 15664.
(31) Du, H.; Liu, L.; Su, L.; Zeng, F. P.; Wang, K. L.; Peng, W. X.; Zhang, H.; Song, T. Q. Seasonal Changes and Vertical Distribution of Fine Root Biomass During Vegetation Restoration in a Karst Area, Southwest China. *Front. Plant Sci.* **2019**, *9* (2001), 2001.
(32) Lu, M.; Du, H.; Song, T.; Peng, W.; Su, L.; Zhang, H.; Zeng, Z.; Wang, K.; Zeng, F. Effects of density dependence in an evergreen-deciduous broadleaf karst forest in southwest China. *Forest Ecology and Management* **2021**, *490*, 119142.
(33) Wang, X.; Yuan, W.; Lin, C.-J.; Wang, D.; Luo, J.; Xia, J.; Zhang, W.; Wang, F.; Feng, X. Root uptake dominates mercury accumulation in permafrost plants of Qinghai-Tibet Plateau. *Communications Earth & Environment* **2022**, *3* (1), 287.
(34) Wang, X.; Yuan, W.; Lin, C. J.; Zhang, L.; Zhang, H.; Feng, X. Climate and Vegetation As Primary Drivers for Global Mercury Storage in Surface Soil. *Environ. Sci. Technol.* **2019**, *53* (18), 10665−10675.
(35) Wang, X.; Yuan, W.; Lin, C. J.; Wu, F.; Feng, X. Stable mercury isotopes stored in Masson Pinus tree rings as atmospheric mercury archives. *J. Hazard Mater.* **2021**, *415*, 125678.
(36) Wang, X.; Yuan, W.; Feng, X.; Wang, D.; Luo, J. Moss facilitating mercury, lead and cadmium enhanced accumulation in organic soils over glacial erratic at Mt. Gongga, China. *Environ. Pollut.* **2019**, *254* (Pt A), 112974.
(37) Sun, R. Y.; Enrico, M.; Heimburger, L. E.; Scott, C.; Sonke, J. E. A double-stage tube furnace-acid-trapping protocol for the pre-concentration of mercury from solid samples for isotopic analysis. *Anal Bioanal Chem.* **2013**, *405* (21), 6771−6781.
(38) Bergquist, B. A.; Blum, J. D. Mass-Dependent and -Independent Fractionation of Hg Isotopes by Photoreduction in Aquatic Systems. *Science* **2007**, *318* (5849), 417−420.
(39) Blum, J. D.; Bergquist, B. A. Reporting of variations in the natural isotopic composition of mercury. *Anal. Bioanal. Chem.* **2007**, *388* (2), 353−359.
(40) Estrade, N.; Carignan, J.; Sonke, J. E.; Donard, O. F. X. Measuring Hg Isotopes in Bio-Geo-Environmental Reference Materials. *Geostand Geoanal Res.* **2010**, *34* (1), 79−93.
(41) Zhou, J.; Obrist, D.; Dastoor, A.; Jiskra, M.; Ryjkov, A. Vegetation uptake of mercury and impacts on global cycling. *Nature Reviews Earth & Environment* **2021**, *2* (4), 269−284.
(42) Yu, B.; Fu, X.; Yin, R.; Zhang, H.; Wang, X.; Lin, C.-J.; Wu, C.; Zhang, Y.; He, N.; Fu, P.; et al. Isotopic composition of atmospheric mercury in China: new evidence for sources and transformation processes in air and in vegetation. *Environ. Sci. Technol.* **2016**, *50* (17), 9262−9269.
(43) Lu, Z.; Yuan, W.; Luo, K.; Wang, X. Litterfall mercury reduction on a subtropical evergreen broadleaf forest floor revealed by multi-element isotopes. *Environ. Pollut.* **2021**, *268* (Pt A), 115867.
(44) Blum, J. D.; Sherman, L. S.; Johnson, M. W. Mercury Isotopes in Earth and Environmental Sciences. *Annu. Rev. Earth Pl Sc* **2014**, *42*, 249−269.
(45) Fu, X. W.; Zhang, H.; Yu, B.; Wang, X.; Lin, C. J.; Feng, X. B. Observations of atmospheric mercury in China: a critical review. *Atmos Chem. Phys.* **2015**, *15* (16), 9455−9476.
(46) Wang, X.; Lin, C. J.; Feng, X. B.; Yuan, W.; Fu, X. W.; Zhang, H.; Wu, Q. R.; Wang, S. X. Assessment of Regional Mercury Deposition and Emission Outflow in Mainland China. *J. Geophys Res-Atmos* **2018**, *123* (17), 9868−9890.
(47) Wu, Q.; Wang, S.; Li, G.; Liang, S.; Lin, C. J.; Wang, Y.; Cai, S.; Liu, K.; Hao, J. Temporal Trend and Spatial Distribution of Speciated Atmospheric Mercury Emissions in China During 1978−2014. *Environ. Sci. Technol.* **2016**, *50* (24), 13428−13435.
(48) Feng, X. B.; Qiu, G. L. Mercury pollution in Guizhou, Southwestern China - An overview. *Sci. Total Environ.* **2008**, *400* (1−3), 227−237.
(49) Feng, X. B.; Shang, L. H.; Wang, S. F.; Tang, S. L.; Zheng, W. Temporal variation of total gaseous mercury in the air of Guiyang, China. *J. Geophys Res-Atmos* **2004**, *109* (D3).
(50) Xia, S.; Yuan, W.; Lin, L.; Yang, X.; Feng, X.; Li, X.; Liu, X.; Chen, P.; Zeng, S.; Wang, D.; Su, Q.; Wang, X. Latitudinal gradient for mercury accumulation and isotopic evidence for post-depositional processes among three tropical forests in Southwest China. *J. Hazard Mater.* **2022**, *429*, 128295.
(51) Chen, J.; Hintelmann, H.; Feng, X.; Dimock, B. Unusual fractionation of both odd and even mercury isotopes in precipitation from Peterborough, ON, Canada. *Geochim Cosmochim Ac* **2012**, *90*, 33−46.
(52) Li, K.; Lin, C. J.; Yuan, W.; Sun, G. Y.; Fu, X. W.; Feng, X. B. An improved method for recovering and preconcentrating mercury in natural water samples for stable isotope analysis. *Journal of Analytical Atomic Spectrometry* **2019**, *34* (11), 2303−2313.
(53) Gratz, L. E.; Keeler, G. J.; Blum, J. D.; Sherman, L. S. Isotopic composition and fractionation of mercury in Great Lakes precipitation and ambient air. *Environ. Sci. Technol.* **2010**, *44* (20), 7764−7770.
(54) Yuan, W.; Wang, X.; Lin, C.-J.; Wu, C.; Zhang, L.; Wang, B.; Sommar, J.; Lu, Z.; Feng, X. Stable Mercury Isotope Transition during

Postdepositional Decomposition of Biomass in a Forest Ecosystem over Five Centuries. *Environ. Sci. Technol.* **2020**, *54* (14), 8739−8749.
(55) Xia, S.; Yuan, W.; Lin, L.; Yang, X.; Feng, X.; Li, X.; Liu, X.; Chen, P.; Zeng, S.; Wang, D.; Su, Q.; Wang, X. Latitudinal gradient for mercury accumulation and isotopic evidence for post-depositional processes among three tropical forests in Southwest China. *J. Hazard Mater.* **2022**, *429*, 128295.
(56) Guedron, S.; Amouroux, D.; Tessier, E.; Grimaldi, C.; Barre, J.; Berail, S.; Perrot, V.; Grimaldi, M. Mercury Isotopic Fractionation during Pedogenesis in a Tropical Forest Soil Catena (French Guiana): Deciphering the Impact of Historical Gold Mining. *Environ. Sci. Technol.* **2018**, *52* (20), 11573−11582.
(57) Blum, J. D.; Sherman, L. S.; Johnson, M. W. Mercury Isotopes in Earth and Environmental Sciences. *Annual Review of Earth and Planetary Sciences* **2014**, *42*, 249−269.
(58) Yuan, W.; Wang, X.; Lin, C. J.; Song, Q.; Zhang, H.; Wu, F.; Liu, N.; Lu, H.; Feng, X. Deposition and Re-Emission of Atmospheric Elemental Mercury over the Tropical Forest Floor. *Environ. Sci. Technol.* **2023**, *57* (29), 10686−10695.
(59) Yuan, W.; Wang, X.; Lin, C. J.; Wu, C.; Zhang, L.; Wang, B.; Sommar, J.; Lu, Z.; Feng, X. Stable Mercury Isotope Transition during Postdepositional Decomposition of Biomass in a Forest Ecosystem over Five Centuries. *Environ. Sci. Technol.* **2020**, *54* (14), 8739−8749.
(60) Zheng, W.; Hintelmann, H. Nuclear Field Shift Effect in Isotope Fractionation of Mercury during Abiotic Reduction in the Absence of Light. *J. Phys. Chem. A* **2010**, *114* (12), 4238−4245.
(61) Zheng, W.; Hintelmann, H. Isotope Fractionation of Mercury during Its Photochemical Reduction by Low-Molecular-Weight Organic Compounds. *J. Phys. Chem. A* **2010**, *114* (12), 4246−4253.
(62) Motta, L. C.; Kritee, K.; Blum, J. D.; Tsz-Ki Tsui, M.; Reinfelder, J. R. Mercury Isotope Fractionation during the Photochemical Reduction of Hg(II) Coordinated with Organic Ligands. *J. Phys. Chem. A* **2020**, *124* (14), 2842−2853.
(63) Sun, R.; Jiskra, M.; Amos, H. M.; Zhang, Y.; Sunderland, E. M.; Sonke, J. E. Modelling the mercury stable isotope distribution of Earth surface reservoirs: Implications for global Hg cycling. *Geochim. Cosmochim. Acta* **2019**, *246*, 156−173.
(64) Luo, K.; Yuan, W.; Liu, N.; Zeng, S.; Wang, D.; Lu, Z.; Wang, X.; Feng, X. Remarkable Variation in the Process of Hg Accumulation in Timberline Forests Indicates an Aggravated Hg Burden in Alpine Forests Under Climate Warming. *Journal of Geophysical Research: Biogeosciences* **2022**, *127* (9), e2022JG006940.
(65) Zheng, W.; Demers, J. D.; Lu, X.; Bergquist, B. A.; Anbar, A. D.; Blum, J. D.; Gu, B. Mercury Stable Isotope Fractionation during Abiotic Dark Oxidation in the Presence of Thiols and Natural Organic Matter. *Environ. Sci. Technol.* **2019**, *53* (4), 1853−1862.
(66) Heckman, K. A.; Possinger, A. R.; Badgley, B. D.; Bowman, M. M.; Gallo, A. C.; Hatten, J. A.; Nave, L. E.; SanClements, M. D.; Swanston, C. W.; Weiglein, T. L.; Wieder, W. R.; Strahm, B. D. Moisture-driven divergence in mineral-associated soil carbon persistence. *Proc. Natl. Acad. Sci. U. S. A.* **2023**, *120* (7), No. e2210044120.
(67) Lavallee, J. M.; Soong, J. L.; Cotrufo, M. F. Conceptualizing soil organic matter into particulate and mineral-associated forms to address global change in the 21st century. *Glob Chang Biol.* **2020**, *26* (1), 261−273.
(68) Lugato, E.; Lavallee, J. M.; Haddix, M. L.; Panagos, P.; Cotrufo, M. F. Different climate sensitivity of particulate and mineral-associated soil organic matter. *Nature Geoscience* **2021**, *14* (5), 295−300.
(69) Quenea, K.; Lamy, I.; Winterton, P.; Bermond, A.; Dumat, C. Interactions between metals and soil organic matter in various particle size fractions of soil contaminated with waste water. *Geoderma* **2009**, *149* (3), 217−223.
(70) Obrist, D.; Johnson, D. W.; Lindberg, S. E.; Luo, Y.; Hararuk, O.; Bracho, R.; Battles, J. J.; Dail, D. B.; Edmonds, R. L.; Monson, R. K.; Ollinger, S. V.; Pallardy, S. G.; Pregitzer, K. S.; Todd, D. E. Mercury Distribution Across 14 US Forests. Part I: Spatial Patterns of Concentrations in Biomass, Litter, and Soils. *Environ. Sci. Technol.* **2011**, *45* (9), 3974−3981.
(71) Kleber, M.; Bourg, I. C.; Coward, E. K.; Hansel, C. M.; Myneni, S. C. B.; Nunan, N. Dynamic interactions at the mineral-organic matter interface. *Nature Reviews Earth & Environment* **2021**, *2*, 402.
(72) Weng, Z.; Lehmann, J.; Van Zwieten, L.; Joseph, S.; Archanjo, B. S.; Cowie, B.; Thomsen, L.; Tobin, M. J.; Vongsvivut, J.; Klein, A.; Doolette, C. L.; Hou, H. E.; Mueller, C. W.; Lombi, E.; Kopittke, P. M. Probing the nature of soil organic matter. *Crit Rev. Env Sci. Tec* **2022**, *52* (22), 4072−4093.
(73) Eklof, K.; Kraus, A.; Weyhenmeyer, G. A.; Meili, M.; Bishop, K. Forestry Influence by Stump Harvest and Site Preparation on Methylmercury, Total Mercury and Other Stream Water Chemistry Parameters Across a Boreal Landscape. *Ecosystems* **2012**, *15* (8), 1308−1320.
(74) Ma, M.; Wang, D. Y.; Du, H. X.; Sun, T.; Zhao, Z.; Wang, Y. M.; Wei, S. Q. Mercury dynamics and mass balance in a subtropical forest, southwestern China. *Atmos Chem. Phys.* **2016**, *16* (7), 4529−4537.
(75) Curtis, P. G.; Slay, C. M.; Harris, N. L.; Tyukavina, A.; Hansen, M. C. Classifying drivers of global forest loss. *Science* **2018**, *361* (6407), 1108−1111.
(76) Fostier, A. H.; Forti, M. C.; Guimaraes, J. R. D.; Melfi, A. J.; Boulet, R.; Santo, C. M. E.; Krug, F. J. Mercury fluxes in a natural forested Amazonian catchment (Serra do Navio, Amapa State, Brazil). *Sci. Total Environ.* **2000**, *260* (1−3), 201−211.
(77) Bushey, J. T.; Driscoll, C. T.; Mitchell, M. J.; Selvendiran, P.; Montesdeoca, M. R. Mercury transport in response to storm events from a northern forest landscape. *Hydrol Process* **2008**, *22* (25), 4813−4826.
(78) Cristol, D. A.; Brasso, R. L.; Condon, A. M.; Fovargue, R. E.; Friedman, S. L.; Hallinger, K. K.; Monroe, A. P.; White, A. E. The movement of aquatic Mercury through terrestrial food webs. *Science* **2008**, *320* (5874), 335−335.
(79) Douglas, T. A.; Loseto, L. L.; Macdonald, R. W.; Outridge, P.; Dommergue, A.; Poulain, A.; Amyot, M.; Barkay, T.; Berg, T.; Chetelat, J.; Constant, P.; Evans, M.; Ferrari, C.; Gantner, N.; Johnson, M. S.; Kirk, J.; Kroer, N.; Larose, C.; Lean, D.; Nielsen, T. G.; Poissant, L.; Rognerud, S.; Skov, H.; Sorensen, S.; Wang, F. Y.; Wilson, S.; Zdanowicz, C. M. The fate of mercury in Arctic terrestrial and aquatic ecosystems, a review. *Environ. Chem.* **2012**, *9* (4), 321−355.

https://doi.org/10.1021/acs.est.3c05409
Environ. Sci. Technol. 2023, 57, 17490−17500